Self-Organization of Mixtures of Fluorocarbon and Hydrocarbon Amphiphilic Thiolates on the Surface of Gold Nanoparticles

Paola Posocco,[†] Cristina Gentilini,[‡] Silvia Bidoggia,[‡] Alice Pace,[‡] Paola Franchi,[§] Marco Lucarini,[§,*] Maurizio Fermeglia,[†] Sabrina Pricl,[†,#,*] and Lucia Pasquato[‡,#,*]

[†]Molecular Simulation Engineering Laboratory (MOSE), DI3, University of Trieste, 34127 Trieste, Italy, [‡]Department of Chemical and Pharmaceutical Sciences, University of Trieste, 34127 Trieste, Italy, [§]Department of Organic Chemistry "A. Mangini", University of Bologna, 40126 Bologna, Italy, and [#]INSTM Trieste Unit, University of Trieste, 34127 Trieste, Italy

ABSTRACT Self-assembled monolayers composed of a mixture of thiolate molecules, featuring hydrocarbon or perfluorocarbon chains (*H*- and *F*-chains) terminating with a short poly(oxoethylene) (PEG) moiety, are the most extreme example of surfactant immiscibility on gold nanoparticles reported so far. The phase segregation between *H*-chains and *F*-chains and the consequent, peculiar folding of PEG chains are responsible for the increased affinity of a selected radical probe for the fluorinated region, which increases as the size of the fluorinated domains decrease, independently of the shape of such domains. This feature has been revealed by ESR measurements and an *in silico* innovative multiscale molecular simulations approach in explicit water. Our results reveal an underlying mechanism of a transmission of the organization of the monolayer from the inner region close to the gold surface toward the external hydrophilic PEG region. Moreover, this study definitively proves that a mixed monolayer is a complex system with properties markedly different from those characterizing the parent homoligand monolayers.

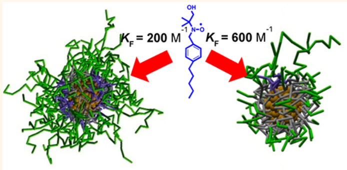

KEYWORDS: ligand morphology · phase separation · self-assembly · gold nanoparticles · multiscale molecular modeling · electron spin resonance

In his review on molecular architecture and function of polymeric oriented systems in 1984, Ringsdorf wrote, "The principle of self-organization for the creation of functional units is not an invention of modern natural sciences ... the self-organization of molecules leads to supramolecular systems and is responsible for their functions."[1] At that time, the focus was on the spontaneous organization of molecules on the micrometer scale. More recently, the interest has shifted to the nanometer scale.[2] As an example, clusters of functional groups on gold nanoparticles (NPs) can elicit catalytic cooperative processes,[3−9] assume the ideal geometry for multivalent recognition,[10,11] or give rise to material with unprecedented properties as revealed by striped NPs.[12,13]

The ability to govern the morphology of NP surfaces is critical for improving the control of the shape of new materials[14−17] and the understanding of their interaction with natural systems such as cell surfaces. This, in turn, will definitely increase the level of comprehension of the mechanisms controlling NP cellular activity.[18]

Gold NPs were shown to be ideal scaffolds to test the self-organization of ligands forming a protective monolayer. The methods for their synthesis are reproducible and allow good control over size, shape, and dispersion. Gold NPs are stable up to 150 °C, and a variety of techniques, generally used for organic compounds (*e.g.*, nuclear magnetic resonance (NMR) and mass spectrometry (MS)), can be employed to characterize NPs with diameters up to 5 nm.[19,20] However, only few suitable methods have been reported so far for the direct "visualization" of the monolayer organization on gold NPs composed of different ligands. Stellacci reported the use of scanning tunnelling microscopy (STM)[21] and more recently atomic force microscopy (AFM)[2] to show how mixed monolayers composed of thiolates of different length self-organize on the gold surface. One limitation to the employment of such techniques is posed by the length of the ligands (so far limited to 14−16 carbon atoms, or an equivalent chain length) or the presence on the nanoparticle surface of charged groups or PEG chains, two moieties very often used to endow NPs with water solubility. X-ray diffraction analysis is the best methodology to determine the precise

* Address correspondence to lpasquato@units.it.

Received for review May 29, 2012 and accepted July 17, 2012.

10.1021/nn302366q

organization of the ligands grafted on the gold surface.[22] However, many limitations exist in this great experimental challenge: the need of a suitable crystal, monodispersity of the NPs, use of rigid ligands, and size of the NP, to mention only a few. For example, the presence of the PEG chains *a priori* prevents the use of such techniques because of the known disordered arrangement of these molecular moieties. For these reasons we applied an indirect method based on ESR[23] spectroscopy using a radical probe sensitive to the polarity of the environment for the study of mixed monolayers composed of amphiphilic thiolates decorated with a terminal PEG chain.[24−26] NMR methods may disclose the presence of Janus particles[27] or, in the presence of binding elements for paramagnetic ions, also a different organization of mixed monolayers.[28] Other indirect methods have relied on reactive proximity probes for chemical cross-linking between two ligands[29] or on a fluorescent anionic probe that reports the presence of three close positive charges[30] or a charged SERS-active porphyrin molecule.[31] Many of these indirect methods, however, suffer from the lack of a general view of the monolayer organization.

From a computational chemistry perspective, previous atomistic and mesoscale simulations have been performed to explain the origin of experimentally observed stripe-like patterns generated by mixtures of short and long ligands coadsorbed on the surface of gold NPs.[32] These studies showed that different parameters such as the chain length of the ligands and/or the presence of charged end groups influence the formation of the striped morphologies and their thickness. In particular, the use of short ligand mixtures resulted in the formation of Janus particle, whereas an increased length difference between unlike ligands caused a decrease of stripe thickness.[33]

Phase separation of *F*- and *H*-chain surfactants was reported for the first time in micellar systems.[34] A few years later, Kunitake[35] described the phase separation of hydrocarbon and fluorocarbon bilayer membranes, while Ringsdorf[36] showed by freeze-fracture electron microscopy that segregation in monolayers and liposomes occurs when the membrane is composed of a mixture of lipids containing *H*- and *F*-chains, even when the two lipids bear the same headgroup. The two types of lipids are immiscible, and domains of individual lipids are formed from the lipid mixture instead of two different liposome populations. Since then, many studies have provided evidence of the phase segregation of compounds with *H*- and *F*-chains.[37−40] AFM investigations of model membranes composed of mixtures of *F*- and *H*- phospholipids reveal an intricate, composition-dependent domain structure consisting of 50 nm stripes interspersed between 1 μm sized domains.[37] The ability of *F*-compounds to spontaneous self-assembly is general and is documented to occur on different materials. For example, hexafluoroleucine residues in a peptide sequence trigger self-association into dimers and higher order aggregates in lipid micelles.[41] Also, the combination of mutually immiscible polymeric compounds in a star block terpolymer with a lipophobic poly(perfluoropropylene oxide) block was shown to be a successful strategy for the formation of multicompartment micelles.[42]

Recently, Singh *et al*. proved that a mixed self-assembled monolayer (SAM) of immiscible ligands is expected to thermodynamically phase-separate into patchy domains, and on substrates with a high degree of curvature such as NPs, the metastable patchy phase evolves into the equilibrium striped phase.[43] The degree of miscibility (expressed through the Flory−Huggins parameter) is one of the two main factors determining the morphology and kinetics of pattern formation in mixed monolayers. Large values of the Flory−Huggins parameter favor a complete phase separation into domains for thermodynamic reasons. From a practical standpoint, the degree of immiscibility can be maximized using a mixture of *F*- and *H* ligands.

We have recently reported the design and synthesis of water-soluble gold NPs coated with a mixture of *F*- and *H*-amphiphilic thiolates (*F*-NPs and *H*-NPs) in different ratios, and preliminary ESR investigations strongly supported the phase segregation of *F*-ligands and *H*-ligands.[44] This study, however, left several open questions on the shape and size of the microphase separate domains as well as on the value of the binding constant of the radical probe with the mixed monolayer, which, apparently, was higher than the corresponding value measured in a homogeneous monolayer of *F*-ligands. These issues can be resolved only by getting a clear picture of how the mixed self-assembled monolayers are organized. NPs decorated by mixtures of the amphiphilic PEG-terminated *F*-ligands and *H*-ligands are not suited to be directly "visualized" by STM for the two main reasons mentioned above: (i) the length of the ligands and, above all, (ii) the presence of the outer layer of disordered PEG chains that prevent distinguishing the two types of underlying thiolates. No other methodologies can unravel the three-dimensional structure of the PEG phase on the NP surface. To gain insight into the mechanisms of the organization of such mixed monolayers, we then resorted to a multiscale molecular simulation approach to predict the self-assembling of the mixed monolayers on gold NPs. According to the *ad hoc* developed ansatz, fully atomistic molecular dynamics (MD) simulations in the explicit presence of water as solvent were performed to retrieve fundamental structural and energetical information at the molecular level. The data gathered by MD simulations were then mapped into the corresponding information required to run coarse-grained simulations at a mesoscopic level using dissipative particle dynamics (DPD)

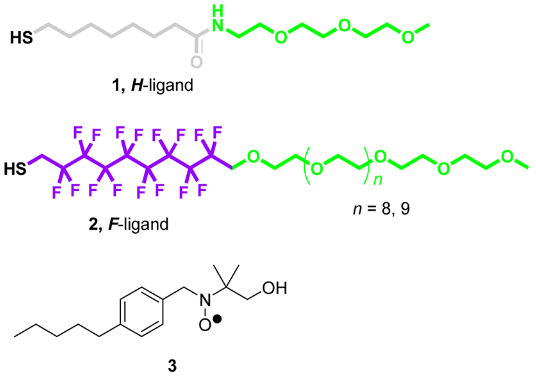

Figure 1. Structures of the *H*- and *F*-ligands and of the radical probe 3.

and to ultimately predict the morphology of the microphase segregation of all systems considered in this work. In order to compare *in silico* results with the ESR experimental evidence, we carried out measurements of the affinity constants of a radical probe in the presence of NPs modified by mixed monolayers of different *F*- and *H*-ligand concentrations. Moreover, to pinpoint the macroscopic differences between homo- and heteroligand monolayers, we further studied mixtures at different ratios of NPs modified by *F*- and *H*-homoligands, respectively, by ESR spectroscopy. In this case, ESR spectroscopy is an appropriate tool to inspect the accessibility to the hydrophobic/lipophobic phase of a suitable probe, which, in turn, depends on the structure of the hydrophilic phase.

RESULTS AND DISCUSSION

NPs coated with homoligands **1**[45] or **2**[26] (see Figure 1) and with mixtures of these thiols[44] were prepared by reduction of the complex Au(I)−ligand with sodium borohydride in homogeneous phase. NPs protected by mixed monolayers were prepared either by direct synthesis, using a blend of thiolates of **1** and **2** or, alternatively, by place-exchange reaction from NPs protected by a homoligand monolayer. We explored both strategies. In the direct synthesis, we observed a competitive grafting of *H*-ligands over *F*-ligands. Indeed, 1:4, 1:1, 4:1, and 8:1 ratios of *H*-ligand to *F*-ligand were used in order to form monolayers with compositions 1:1, 2.5:1, 4:1, and 20:1, respectively. This can be explained considering the lower nucleophilicity of the *F*-thiolate molecule (induced by the electron-withdrawing effect of the *F*-chain) compared to that of the *H*-ligand used to form the respective Au(I)−ligand complexes. NPs protected by a 1:1 mixture of *H*-ligands and *F*-ligands were prepared by exchange of the thiolate chains of **2** with thiol **1** for 3 days in a methanol solution at 28 °C. The samples used in the present study are reported in columns 1−4 of Table 1, together with the relevant NP composition, the size of the NP metal core, and the molar fraction of the monolayers.

For the prediction of the morphology and the average dimensions of the mixed-monolayer-protected NPs we then employed an innovative approach based on the multiscale molecular modeling (M3) procedure. Specifically, all energetical and structural information stemming from atomistic-level MD simulations were exploited to predict in detail the organic molecule chain distribution around the Au NP cores at a nanometer scale in the explicit presence of water as the solvent. The computational recipe was validated applying the same, *ad hoc* developed procedure to NPs functionalized by mixtures of ligands with chemical nature and structure closely related to those considered in the present work and recently synthesized and characterized by Stellacci *et al.*[46] (see Figure S3 and Supporting Information for details). The excellent agreement between the experimentally detected morphology of these reference monolayer systems and the prediction yielded by our computational procedure confirmed both the validity and the reliability of the proposed approach.

The last two columns of Table 1 highlight the morphologies of the self-assembled monolayers protecting gold NPs obtained from DPD simulations performed according to our M3 approach as a function of the relative molar fraction of the two ligands. As somewhat expected,[12,19] the relative composition of the ligand mixture plays a substantial role in determining the arrangement of the relevant SAM. Indeed, in the presence of an equimolar mixture of the two ligands (*i.e.*, system **5a**), the *H*- and *F*-chains undergo a phase segregation, ultimately resulting in alternate domains with stripe morphology, each extending along the entire diameter of the NP (**5a** in Table 1). The estimated average dimensions of these domains range between 0.6 and 0.7 nm.

Interestingly, although system **5b** is characterized by the same composition as system **5a**, the resulting SAM morphology is no longer organized in stripes but has evolved toward a complete segregation, or, in other terms, results in a Janus nanoparticle (**5b** in Table 2). This finding is not surprising if we consider the fact that, in the case of system **5b**, the NP core diameter is considerably smaller than that of NP **5a**: 1.6 and 2.2 nm, respectively. Thus, the role of the NP curvature on the morphology of the self-assembled monolayer is more pronounced for system **5b** than for system **5a**. Notably, quite a similar effect was already detected and discussed for gold NPs functionalized by a 2:1 molar mixture of 1-nonanethiol and 4-methylbenzenethiol.[47]

By increasing the relative percentage of *H*-ligands with respect to *F*-ligands ($\chi = 0.71$), the phase separation originates a variegated pattern on the NP surface, where stripe- and patch-like segregation domains of both chemical species coexist (system **6** in Table 2). If the molar fraction is further increased (0.80 and 0.95, respectively), the corresponding number of fluorocarbon chains is too small to yield stripe-like domains. Nevertheless, the *F*-chains still aggregate, originating

TABLE 1. Characteristics of the Gold NPs Coated with Mixtures of Thiolates of 1 and 2 and Ligand Organization on the Surface of Gold NPs at Different Molar Fraction of the Two Ligands[a]

NPs	χ^{a}	Core diameter (nm)[b]	NPs Composition[c]		
4	0	2.5 ± 0.8	$\mathrm{Au}_{590}\boldsymbol{F}_{80}$	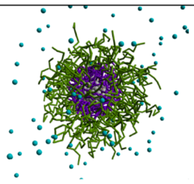	
5a	0.5	2.2 ± 0.4	$\mathrm{Au}_{400}\boldsymbol{H}_{54}\boldsymbol{F}_{54}$	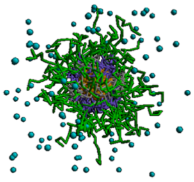	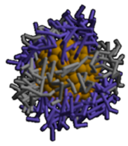
5b[d]	0.5	1.6 ± 0.2	$\mathrm{Au}_{150}\boldsymbol{H}_{33}\boldsymbol{F}_{33}$	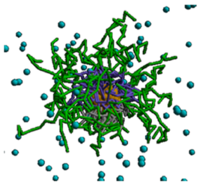	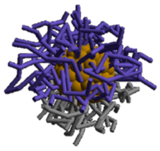
6	0.71	2.5± 0.4	$\mathrm{Au}_{540}\boldsymbol{H}_{108}\boldsymbol{F}_{43}$	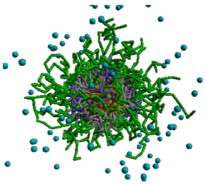	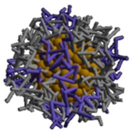
7	0.80	1.9± 0.2	$\mathrm{Au}_{230}\boldsymbol{H}_{66}\boldsymbol{F}_{16}$	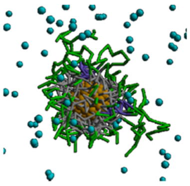	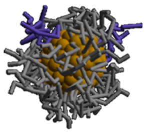
8	0.95	1.9± 0.3	$\mathrm{Au}_{240}\boldsymbol{H}_{68}\boldsymbol{F}_{3}$	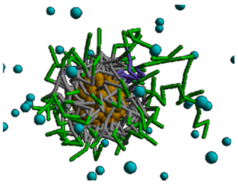	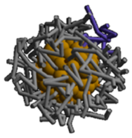
9	1	1.5± 0.3	$\mathrm{Au}_{102}\boldsymbol{H}_{50}$	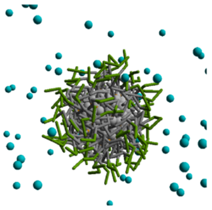	

[a] In the left panel images, the hydrophilic poly(ethylene oxide) component of the ligands is shown explicitly, while in the right panel images only the *F*- and *H*-moieties of the ligands are depicted to highlight the monolayer morphological organization. Color code: green, PEG; gray, *H*-chain; purple, *F*-chain; brown, NP gold core. In the left panel images, a number of water molecules are also shown as turquoise spheres. Sphere radii not drawn to scale. [b] Molar fraction of the *H*-ligand forming the monolayer determined by integration of ^{1}H NMR signals pertaining to the thiolate chains of **1** and to thiolate chains of **2** on decomposed NPs. [c] Average core diameter by TEM measurements of at least 190 NPs. [d] Estimated composition based on TEM and TGA analysis and considering the monolayer composition determined by ^{1}H NMR on decomposed NPs. [e] Prepared from *F*-NPs by place-exchange procedure.

small patches interspersed in a matrix of *H*-chains (samples **7** and **8** in Table 1).

Other interesting information gathered from the present simulations concerns the distribution of the

PEG-modified *H*-/*F*-chains around the NP gold core in an aqueous environment. Figure 2 shows the radial distribution functions of the SAM components for system **5a** as an example. As can be inferred from Figure 2, on average the *H*-chains extend into the aqueous medium by approximately 1.59 nm (±0.12 nm), while the *F*-ligands reach 2.60 nm (±0.10 nm). However, both these molecular dimensions are well below the corresponding fully stretched lengths, *i.e.*, 2.28 and 5.46 nm, respectively. This is supported by simulations of homoligand NPs **4** and **9**, whose morphologies are depicted in Table 1 and in Figure S4. For the first homoligand system considered, **4**, the average shell thickness of the NP was calculated to be equal to 2.82 nm (±0.11 nm), whereas for the second homoligand nanoparticles, **9**, the corresponding value was estimated to be equal to 1.40 nm (±0.10 nm). If compared with the corresponding mixed homoligand system **5a**, it is apparent that the small ligand chains somewhat stretch out toward the longer ones and these, in turn, bend over the smaller counterparts. Notably, in the mixed monolayers the PEG moiety of both chain types concur in the formation of a sort of hydrophilic shell, which surrounds the overall NP and screens the underlying hydrophobic components from the unfavorable interaction with water. It is interesting to observe also that, in the case of both the *H*-chain and *F*-chain, the PEG residues are endowed with a considerable degree of flexibility, which allows this moiety to penetrate within the hydrophobic domains and, from time to time during the simulation, to extend to the NP core. Further, as evidenced from the full nanoparticle simulation images shown in the third column of Table 1, the PEG shell is not entirely homogeneous, but the PEG chains do seem to loosely aggregate on top of the corresponding underlying domains.

TABLE 2. Equilibrium Constants (T = 298 K) and ESR Parameters in the Presence of Heteroligand Mixed Monolayers

χ	K_{mix}/M^{-1}	$\Delta G/G^{d}$	K_H/K_F^{e}	K_F/M^{-1}	K_H/M^{-1}
0	176[a]	2.05 (2.05)		176[a]	
0.50	100 ± 7.7[b]	2.05 (1.82)	<0.04	200	<10
0.71	100 ± 8.1	2.05 (1.69)	<0.04	350	<10
0.80	189 ± 20	1.92 (1.60)	0.06	762[f]	45[f]
0.95	120 ± 11	1.54 (1.45)	0.16	600[f]	96[f]
1	104[c]	1.40 (1.40)			104[c]

[a] From ref 26. [b] Errors refer to twice the standard deviation. [c] From ref 25. [d] Determined by ESR. In parentheses the theoretical value calculated by using eqs 1 and 2 with $K_H/K_F = 0.59$. [e] Determined by the experimental values of ΔG. [f] Determined by solving eqs 1, 3, and 4, simultaneously.

To gain further insight into the mechanisms leading to phase separation of our thiol ligands, as a proof of concept we performed a further set of simulations on systems having the following, constant features: NP diameter value of 2.2 nm, ligand mixture composition 1:1, and total number of ligands equal to 108. Accordingly, the influence of the PEG chain and of the ligand chain length could be evaluated. These new systems were modeled according to the procedure adopted for samples **1**−**8** and are summarized in Table S2, while, for an intuitive observation, the relevant DPD snapshots are presented in Figure S5. These simulations show that the shape of the domains is trigger by the total length of the *F*- and *H*-ligands. Indeed, for a monolayer composed of ligands of the same length the resulting microphase segregation consists in a Janus pattern, in agreement with previous studies on related systems,[32,33] while a difference in the total length leads to stripe-like domains.

From an experimental perspective, several years ago[23−26] we set up ESR spectroscopy experiments to investigate the properties of 3D-SAM. The radical probe we used in our studies is *para*-pentyl benzyl hydroxyalkyl nitroxide **3** (Figure 1). In the presence of NPs, the ESR spectrum of **3** is characterized by two sets of signals (see Figure 3) due to the radical partitioning in the monolayer in equilibrium with the free nitroxide in water. The two species are easily distinguishable because (i) at room temperature the exchange between the nitroxide partitioned between the monolayer and the free form is comparable to the EPR time-scale, resulting in separate signals for the two radical species; (ii) both values of a(N) and a(2H$_{\beta}$) (16.25 and 10.14 G in water, respectively) decrease considerably when the aminoxyl is located in the less polar environment of the monolayer.[23] The reduction of the coupling constants has been attributed to the larger weight in media of

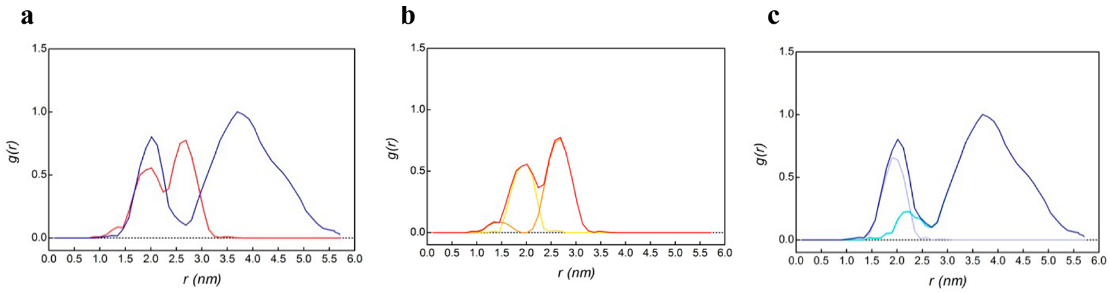

Figure 2. Radial distribution functions (RDFs) for the SAM components of system 5a. (a) Overall RDF for *H*- (red) and *F*- (blue) chains. (b) Overall (red), alkyl (yellow), and PEG moieties (orange) of the RDF for the *H*-chains. (c) Overall (blue), fluorinated (light blue), and PEG moieties (turquoise) of the RDF for the *F*-chains.

Figure 3. ESR spectrum of 3 recorded in water in the presence of an equimolar mixture (28 mM) of homoligand NPs: *F*-NPs 4 and *H*-NPs 9.

low polarity of the nitroxide mesomeric forms, in which the unpaired electron is localized on the oxygen rather than on the nitrogen atom.

Accordingly, we applied the same ESR-based approach to the experimental investigation of the homoligand monolayers containing *H*-ligands or *F*-ligands and found that the radical probe **3** has a greater affinity for the fluorinated monolayer. Also, different splitting constants are observed depending on the nature of organic ligands.[23] In particular, the values of both $a(\mathrm{N})$ and $a(2\mathrm{H}_\beta)$ are substantially smaller when the radical is partitioned in a homoligand monolayer composed of *F*-thiolates ($a(\mathrm{N}) = 15.46$ G, $a(2\mathrm{H}_\beta) = 8.68$ G) compared to the values measured when **3** is in a homoligand monolayer of *H*-ligands ($a(\mathrm{N}) = 15.67$ G, $a(2\mathrm{H}_\beta) = 8.97$ G).[24,26] Once again, this difference in the ESR parameters is attributed to the reduced polarity of the environment experienced by the nitroxide function when dissolved in the fluorinated amphiphilic monolayer with respect to that experienced in the presence of the *H*-ligand.

When the radical probe is located in a mixed monolayer consisting of *F*-ligands and *H*-ligands, the differences in the values of the hyperfine splitting constants are not sufficient to permit the resolution of the spectra due to the radicals partitioned in the two phases. The corresponding ESR spectrum still consists of two sets of peaks: one is due to the spin probe in the aqueous phase; the other one is a superposition of peaks from the radical partitioned in the different monolayer environments.[44]

At the same time, however, the differences in the splitting constants are large enough to result in a notable variation of the corresponding apparent overall splitting of the spectral lines. In particular, the field separation (ΔG) between the low-field lines due to radical **3** partitioned in water (which resonates always at the same field value and can thus be considered as a field marker) and in the monolayer (see Figure 3) decreases from 2.05 *G* when the spectrum is recorded in the presence of *F*-NPs to 1.40 G in the presence of *H*-NPs. As a consequence, any variation in the amount of the radical partitioned in the two phases should reflect a change of the corresponding value of ΔG. The black curve in Figure 4 shows the dependence of ΔG as a function of monolayer composition χ (*i.e.*, the molar fraction of *H*-ligands) in mixed monolayer-protected nanoparticles.[44]

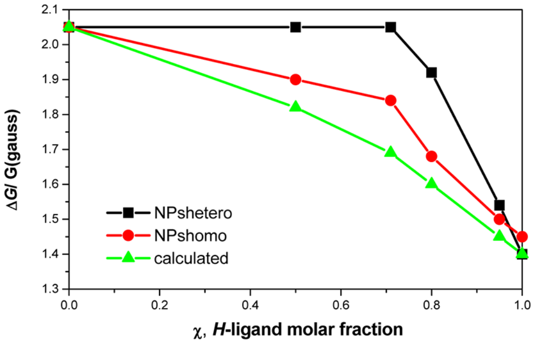

Figure 4. Dependence of ΔG (in gauss) as a function of monolayer composition. Black curve: NPs containing mixed monolayers; red curve: mixtures of homoligand NPs. The green curve is the theoretical behavior calculated by using eqs 1 and 2 with $K_\mathrm{F} = 176\ \mathrm{M}^{-1}$ and $K_\mathrm{H} = 104\ \mathrm{M}^{-1}$.

For values of $\chi \leq 0.71$, ΔG is nearly independent of the thiol composition and equivalent to the value found when the radical is located in a homoligand monolayer containing only *F*-thiolates. In agreement with the computational results discussed above, the equivalence of the spectroscopic parameters can be interpreted as evidence that, triggered by the lipophobicity of perfluorocarbons,[44] heteroligand 3D SAMs phase-separate into domains of homoligands. Indeed, according to our DPD simulations, NPs **5a**, **5b**, and **6** are characterized by the presence of *F*-domains extended enough to guarantee to the probe an environment populated by *F*-ligands only. Because of the higher affinity of the radical probe for the fluorinated monolayer, the nitroxidic probe is partitioned exclusively in these fluorinated domains. Decreasing the amount of *F*-ligands (*i.e.*, for $\chi = 0.80$ and 0.95, corresponding to NPs **7** and **8** in Table 1), the probe experiences an environment composed mainly, but not exclusively, of *F*-ligands ($\Delta G =$ 1.92 G, NP **7**) or of three *F*-ligands only (NP **8**),[48] in agreement with the corresponding simulations showing only one domain composed of *F*-thiolates in the monolayer. The ΔG is a complex parameter influenced by the affinity constants of the probe for the *F*-/*H*-domains and, consequently, by the concentration of the two types of ligands as discussed below.

On condition that the structures of homoligand islands in the mixed monolayer are approximately the same as those in the pure phase of homoligand NPs, the theoretical variation of ΔG with the *H*-ligand molar fraction can be predicted by eqs 1 and 2,[49] using the known values of the affinity of the probe for the *F*- and *H*-phases, respectively:

$$\Delta G = 1.40X_\mathrm{H} + 2.05(1 - X_\mathrm{H}) \qquad (1)$$

$$X_\mathrm{H} = \frac{\dfrac{K_\mathrm{H}[\textbf{\textit{H}-ligand}]}{K_\mathrm{F}[\textbf{\textit{F}-ligand}]}}{1 + \dfrac{K_\mathrm{H}[\textbf{\textit{H}-ligand}]}{K_\mathrm{F}[\textbf{\textit{F}-ligand}]}} \qquad (2)$$

In eq 1, X_H represents the molar fraction of the radical probes located in the NP monolayer that are surrounded by *H*-chains, while $1 - X_H$ is the molar fraction of those experiencing the *F*-chain environment. X_H is related to the affinity constants of the probe for the two phases, K_F and K_H, by eq 2. The ΔG dependence on monolayer composition calculated using the above equations, with $K_F = 176\ M^{-1}$ and $K_H = 104\ M^{-1}$,[25,26] is shown as a green curve in Figure 4. It is evident that the experimental data (black curve) deviate significantly from the theoretical model predicted by eqs 1 and 2. Since this model is based on the assumption that the probe affinity for the separated domains in the heteroligand NPs and for the pure phases in the homoligand NPs is approximately the same, the results shown in Figure 4 clearly indicate that this condition is not fulfilled in the present case. In other words, the properties of the separated domains in the mixed monolayers cannot be predicted from the knowledge of the properties shown by the individual homoligand monolayers.

In order to determine the real affinities of the probe for the separated domains in the heteroligand monolayers, we then recorded a new series of ESR spectra of **3** in the presence of different concentrations of protected NPs. Since in heteroligand monolayers the radical probes can be partitioned simultaneously in *H*- and *F*-domains, plotting the ratio of the concentration of the probe located in the monolayer and of the free species in water (obtained by simulation of the ESR spectra)[50] as a function of the total concentration of thiolates (Figure S6) affords an overall affinity constant K_{mix} as in eqs 3 and 4:

$$\frac{[\mathbf{3}]_{\text{monolayer}}}{[\mathbf{3}]_{\text{water}}} = K_{\text{mix}}\{[F\text{-ligand}] + [H\text{-ligand}]\} \qquad (3)$$

$$K_{\text{mix}} = K_F X_{F\text{-ligand}} + K_H X_{H\text{-ligand}} \qquad (4)$$

When χ is equal to 0.50 and 0.71, the ΔG value determined by ESR measurements indicates that the radical located in the monolayer is actually completely partitioned in the fluorinated phases ($X_H \approx 0$, $X_F \approx 1$). Under this condition, K_F is equal to the overall affinity constant K_{mix} and can be determined directly from the ESR spectra.

Inspection of K_F values reported in Table 2 indicates that they are significantly higher with respect to those measured in the homoligand monolayer of NPs **4**, this increase being larger in the presence of larger amounts of *H*-ligands in the monolayer. It is evident, from the experimental data reported in Table 2, that the relative composition of the ligand mixture plays a substantial role in determining the probe affinity for the mixed monolayer. Indeed, mesoscale simulations show that the underlying segregation morphology and the outer PEG shell organization are such that the probe experiences an energetically favored permeation to reach the lipophobic phase with respect to the homoligand *F*-monolayer. This evidence further supports the conclusion that the properties of the separated domains in the mixed monolayers cannot be predicted from the knowledge of the properties shown individually by the homoligand monolayers. Previous works demonstrate that surface properties of NPs protected by structured mixed monolayers such as the wetting behavior[51] and permeation of cell membranes[12] of particles protected by mixed monolayers are different from the surface features of NPs protected by a single-component monolayer or a disordered mixed monolayer. Here we show that this property is pervasive; that is, it is not limited to the surface of the NP but extends to the entire monolayer.

TABLE 3. ESR Parameters in the Presence of Homoligand NP Mixtures

[*F*-ligand]/mM[a]	[*H*-ligand]/mM[a]	χ	$[3]_{\text{monolayer}}/[3]_{\text{water}}$[b]	ΔG/G[c]
56	0	0	9.9 (9.8)	2.05 (2.05)
28	28	0.5	8.1 (7.8)	1.90 (1.82)
16	40	0.71	7.4 (7.1)	1.84 (1.69)
11	44	0.80	6.7 (6.5)	1.68 (1.60)
2.7	53	0.95	6.0 (6.1)	1.50 (1.45)
0	56	1	6.0 (6.0)	1.45 (1.40)

[a] The concentration refers to ligands bound to NPs (no free ligands present in solution). [b] Determined by ESR. In parentheses the theoretical value calculated by using eq 5 with $K_F = 176\ M^{-1}$ and $K_H = 104\ M^{-1}$. [c] Experimental values determined by ESR. In parentheses the theoretical value calculated by using eq 1 with $K_H/K_F = 0.59$.

The observation that the radical located in the monolayer is *de facto* completely partitioned in the fluorinated phases has another important consequence: the affinity of the probe for the hydrocarbon portion of the monolayer is significantly smaller with respect to the values measured in the homoligand monolayer of NPs **9**. By considering the uncertainty associated with the ESR measure of ΔG (±0.05 G), we can fix an upper limit of $10\ M^{-1}$ for K_H. This value is significantly smaller with respect to the values measured in the homoligand monolayer of NPs **9**. Actually, higher values of K_H should result in a value of ΔG smaller than 2.05 G. When χ equals 0.50 and 0.71, mesoscale simulations show that the transfer of the probe from the aqueous phase to the interior of the *H*-domains required the search for a suitable spot on the surface among PEG chains of *F*-ligands. Thus, the screening of the underlying *H*-ligands by *F*-ligands is expected to significantly increase the energy barrier for the partition of the probe in the hydrocarbon domains.

In the presence of a larger amount of hydrocarbon chains ($\chi > 0.71$, NPs **7** and **8** in Table 1) the field separation (ΔG) between the lines of the radical partitioned in water and in the monolayer starts to decrease, indicating that the probe experiences a monolayer containing also hydrocarbon ligands. This has been attributed to the simultaneous presence of radicals partitioned in *H*- and *F*-domains. Under this condition, the relative amount of the radicals located in the *H*- and *F*-domains (X_H and X_F, respectively) can be obtained by the measure of the value of ΔG. Using these values, and solving simultaneously eqs 2 and 4, the corresponding values of K_F and K_H can be obtained, as shown in Table 3 for the cases when χ is equal to 0.80 and 0.95. K_F reaches a very high value if compared to the value measured in the presence of homoligand nanoparticle.[52] It is also evident from Table 2 that the affinity for the hydrocarbon phase increases with increasing the relative amount of the hydrocarbon chains, approaching the value found in the presence of homoligand NPs when $\chi = 0.95$.

To check the reliability of the ESR experimental results, we recorded ESR spectra of **3** in the presence of solution mixtures containing different ratios of homoligand NPs made of *F*-NPs and *H*-NPs as a control. Under this condition, each homoligand NP is expected to maintain its own properties and the observed ΔG values should be correctly predicted by means of eq 1. Concomitantly, the ratio between the concentration of the probe located in the monolayer and that of the free species in water should be reproduced by eq 5 by setting $K_F = 176$ M^{-1} and $K_H = 104$ M^{-1}.

$$\frac{[\mathbf{3}]_{\text{monolayer}}}{[\mathbf{3}]_{\text{water}}} = K_F[F\text{-ligand}] + K_H[H\text{-ligand}] \qquad (5)$$

These results are summarized in Figure 4 (red curve) and Table 3. The data reported in Table 3 show that, in the presence of homoligand NPs, the ratio between the concentration of the probe located in the monolayer and that of the free species in water is indeed correctly predicted by using $K_F = 176$ M^{-1} and $K_H = 104$ M^{-1}. The ΔG values (Figure 4, red curve) appreciably move toward those obtained with heteroligand NPs, although a sizable difference between them is still present. At the moment, the origin of this discrepancy is unclear.

This last set of experimental evidence ultimately confirms that the properties of the separated domains in the mixed monolayers are different from the properties shown by each individual homoligand monolayer.

CONCLUSIONS

In conclusion, this work presents and discusses the results obtained by a combined experimental/simulation approach to the characterization of gold nanoparticles decorated by immiscible ligands of hybrid nature, *i.e.*, *F*- and *H*-based thiolates bearing a PEG chain as end group. The novel multiscale molecular modeling approach for the simulation of mixtures of ligands grafted on the surface of NPs becomes a powerful tool to predict the morphology of self-assembled monolayers. Moreover, these calculations offer a molecular-based rational for the corresponding experimental ESR results.

The phase segregation between *H*-chains and *F*-chains and the different length of the hydrophilic chains determine the peculiar folding of PEG moieties responsible for the increased affinity of an organic compound for the fluorinated region, which increases as the size of the fluorinated domains decreases, independently of the shape of such domains. In other words, the spontaneous organization of the *F*-/*H*-chains in the inner part of the monolayer is transferred to the outer surface of the NP. These results offered another example that mixed monolayers present features that are different from those of the parent homoligand monolayers.

Additionally, we can summarize the final picture of the monolayer morphologies for the different composition of the mixed monolayer investigated as follows:

(i) Phase segregation occurs for all molar fractions considered, even when about three *F*-chains (4%) are present in the monolayer, the phase segregation being induced by the strong lipophobicity of the *F*-chains. Random distributions, as observed with other mixtures of thiolates on gold NPs,[7,12] are not formed using the mixtures of the *F*- and *H*-thiolates considered in this work.

(ii) The shape of the domains is triggered by the length of the ligands as a consequence of the optimum balance between enthalpic and entropic force.

(iii) The size of the NP core is also a determining factor: below 2 nm Janus domains are formed, whereas stripe-like domains spontaneously form for larger NPs.

(iv) The shape of the phase-segregation domains is also dependent on the composition of the mixed monolayer. For *H*-chains of mole fraction 0.71, a borderline situation is present in which stripe- and patch-like domains coexist. As the molar fraction of the *H*-ligand increases further, the *F*-ligands organize into patches.

The present results show that mixtures of *H*-ligands and *F*-ligands of different length are ideal to control the morphology of mixed self-assembled monolayers in three dimensions. The parameters that enable such a control are relatively easy to tune, and the work illustrated here can thus act as a guide in the formulation of general rules to pattern 3-D monolayers.

We believe that our contribution will stimulate the application of NPs protected by mixed monolayers of selected morphologies for the creation of new materials, more efficient cooperative catalysts, improved multivalent systems to control and understand the interactions with cellular surfaces,[18] and, ultimately, NPs of unprecedented complexity for applications in medicine.

METHODS

General Procedures. NMR spectra were recorded on a Varian 500 MHz spectrometer (operating at 500 MHz for ^{1}H), a Jeol GX-400 MHz (operating at 400 MHz for ^{1}H), and a Bruker Avance 300 MHz (operating at 282 MHz for ^{19}F) using $CDCl_3$ as deuterated solvent. ^{1}H NMR spectra were referenced to the residual protons in the deuterated solvent. Data are reported as follows: chemical shifts are in ppm in the δ scale; multiplicity (s: singlet, d: doublet, t: triplet, q: quartet, br: broad band); integration; assignment. ^{19}F NMR spectra were referenced to trifluorotoluene as external standard. FTIR spectra were recorded using a Thermo Nicolet Avatar 320 FT-IR spectrophotometer on NaCl disks. UV−visible spectra were collected on a UV−vis Unicam Heλios β spectrophotometer. All reagents were purchased from Aldrich and used without further purification. Dry solvents were obtained from Fluka. Chlorinated solvents were stirred over K_2CO_3 for at least 24 h prior to use. All other solvents were reagent grade and used as received.

TGA Analysis. TGA analysis was performed on TGA Q-500 V6.3 Build 189 using a heating rate of 10 °C/min up to 1000 °C.

TEM Analysis. TEM images were obtained with a Jeol 3010 high-resolution electron microscope (1.7 nm point-to-point) operating at 300 keV using a Gatan slow-scan CCD camera (model 794). TEM samples of protected gold nanoparticles were prepared by placing a single drop of 0.5 mg/mL 2-propanol dispersion onto a 200-mesh copper grid coated with an amorphous carbon film. The grid was then dried in air for 24 h. Depending on the Au core size, magnifications between 250.000 and 600.000 were used for counting purposes. Diameters were measured manually using Gatan Digital Micrograph (ver. 3.4.1) software.

ESR Measurements. Radical **3** was generated by mixing 0.5 μL of a methanol solution containing the corresponding amine (0.1 M) and 0.5 μL of a water solution containing Oxone (0.1 M) with 100 μL of a water solution containing variable amounts of NPs. Samples were transferred in capillary tubes (diameter 1 mm) and then placed inside the thermostated cavity of the EPR spectrometer. EPR spectra were recorded using a Bruker ELEXYS E500 spectrometer equipped with an NMR gaussmeter for field calibration and a microwave frequency counter for *g*-factor determination.

Synthesis of *H*-NP. $HAuCl_4 \cdot 3H_2O$ (80 mg, 0.203 × 10^{-3} mol) was dissolved in 40 mL of distilled water and poured into a 250 mL round-bottom flask. A solution of HS-C8-TEG (131 mg, 0.406 × 10^{-3} mol) in deoxygenated dry methanol (41 mL) was added. The solution turned from yellow to orange; the mixture was left to stir for 30 min, while its color faded on standing. The solution was cooled to 0 °C and kept at that temperature for 30 min; further fading was observed. $NaBH_4$ (92 mg, 2.43 × 10^{-3} mol) in 23 mL of water was added in 10 s at 0 °C; the reaction mixture turned immediately deep brown. It was stirred at 0 °C for 30 min and then at room temperature for 3 h. The solvent was removed under reduced pressure without heating above 35 °C. The residue was dissolved in 4 mL of dichloromethane and transferred in two centrifuge tubes, where it was dried under a mild argon flow. The NPs were purified by centrifugation (10 min, 4000 rpm, 20 °C) with diethyl ether (5 × 25 mL) followed by decanting of the supernatant solution. The NPs were further purified by gel permeation chromatography (Sephadex LH-20, methanol). A 71 mg amount of *H*-NPs was obtained as a deep brown solid. ^{1}H NMR (400 MHz, $CDCl_3$): δ 1.31 (br, CH_2); 1.60 (br, CH_2); 2.26 (br, CH_2CO); 3.37 (br, CH_3O); 3.54 (br, CH_2O); 3.62 (br, CH_2O). UV−vis (MeOH, c = 0.1 mg/mL): monotonic decay from 200 nm. TEM: average diameter = 1.5 nm; σ = 0.3 nm; n = 190. TGA: 45.58%. Average composition: Au_{102}(S-C8-TEG)$_{50}$.

Synthesis of *F*-NPs. $HAuCl_4 \cdot 3H_2O$ (25 mg, 0.063 × 10^{-3} mol) was dissolved in 12.5 mL of deoxygenated distilled water and poured into a 100 mL round-bottom flask. A solution of sodium 2,2,3,3,4,4,5,5,6,6,7,7,8,8,9,9-hexadecafluoro-10-(methoxy-PEG550)-decan-1-thiolate (0.139 × 10^{-3} mol) in deoxygenated dry methanol (24.33 mL) was added to the mixture through a double-tipped needle under an argon atmosphere. The reaction mixture turned from yellow to deep orange. The solution was stirred at room temperature for 1 h; then 1.80 mL of an aqueous solution of $NaBH_4$ (27 mg, 0.718 × 10^{-3} mol) was added in 10 s at room temperature. The solution turned from orange to deep brown, suggesting the formation of small protected NPs. The mixture was left to stir for 3 h; then the solvent was removed under reduced pressure. The residue was dissolved in 4 mL of dichloromethane and transferred to two centrifuge tubes, where it was dried under a mild argon flow. The NPs were purified by centrifugation (10 min, 4000 rpm, 20 °C) with diethyl ether (5 × 15 mL) followed by decanting of the supernatant solution. A total of 23 mg of NPs *F*-NPs was obtained as a deep brown solid. ^{1}H NMR (500 MHz, $CDCl_3$): δ 3.3 (br, CH_3O); 3.5−3.7 (br, CH_2O); 4.0 (br, CH_2CF_2O). UV−vis (MeOH, c = 0.1 mg/mL): monotonic decay from 200 nm. TEM: x_m = 2.5 nm; σ = 0.8 nm; n = 442. TGA: 41.86%. Average composition: Au_{590}(S-F8-PEG)$_{80}$.

General Procedure for the Synthesis of Mixed Monolayer NPs. A 0.015 M solution containing a mixture of sodium thiolates of **1** and **2** (2 equiv with respect to Au moles) in deoxygenated methanol was added through a double-tipped needle, under an argon atmosphere, to a solution of $HAuCl_4 \cdot 3H_2O$ in distilled water (2 mg/mL). The reaction mixture was stirred at room temperature for 1 h. Then, 11.4 equiv of a solution 0.4 M $NaBH_4$ in distilled water was added in 10 s. The solution color turned deep brown, suggesting formation of small protected NPs. The mixture was left under stirring 3 h; then the solvent was removed under reduced pressure. The residue was transferred into a centrifuge tube, dispersed in Et_2O, and repeatedly washed (7 × 20 mL) by centrifugation at 4000 rpm to remove unbound thiols. The precipitate was recovered as a brown solid.

For the synthesis of NPs protected by a mixed monolayer, samples **5a** and **6**−**8** with the following ratios between *H*- and *F*-ligands have been used: 1:4, 1:1, 4:1, and 8:1 in order to form monolayers with the following compositions: 1:1, 2.5:1, 4:1, and 20:1, respectively.

Synthesis of NPs 5b through Place-Exchange Reaction. To a solution of 17 mg of *F*-NPs dissolved in 19 mL of dry, deoxygenated methanol, under an argon atmosphere, was added a solution of 3 mg of thiol 1 (9.4 mmol) in 1 mL of methanol, and the mixture was kept at 28 °C for 72 h. The solvent was removed under reduced pressure, and the residue was dispersed in Et_2O and repeatedly washed (7 × 20 mL) by centrifugation at 4000 rpm. A total of 15 mg of NPs was obtained as a brown solid. ^{1}H NMR ($CDCl_3$, 400 MHz): δ 1.1−1.6 (br, CH_2); 2.2 (br, CH_2CO) 3.3 (br, CH_3O); 3.5−3.6 (br, CH_2O); 4.0 (br, CF_2CH_2O). TEM: average diameter = 1.6 nm; σ = 0.2 nm; n = 300. TGA: 59%. Average composition: Au_{150}(SC8TEG)$_{33}$(SF8PEG)$_{33}$.

Conflict of Interest: The authors declare no competing financial interest.

Supporting Information Available: Simulation details: atomistic models, atomistic MD simulations, DPD theory, matching of atomistic (MD)/mesoscale (DPD) pair correlation function, DPD models and details, validation of the procedure, simulations of Au NPs protected by homoligands, NP **4** and NP **9**, parametric simulations. Plot for determination of K_{mix} from ESR measurements, theoretical simulation of ESR low-field lines, and theoretical field separation ΔG as a function of the molar fraction of the radical probes located in the NP monolayer. This material is available free of charge *via* the Internet at http://pubs.acs.org.

Acknowledgment. This work is dedicated to the memory of Professor Giorgio Modena. The authors thank Professors Paolo M. Scrimin and Leonard J. Prins for stimulating discussions. Financial support from the Progetto Regione NANOCANCER (L.P.) and from MIUR, Contract 2008KRBLP5 (P.F., M.L.), is gratefully acknowledge. P.P., M.F., and S.P. are grateful to Dr. Jan-Willem Handgraaf for his technical assistance and fruitful suggestions.

REFERENCES AND NOTES

1. Ringsdorf, H.; Schlarb, B.; Venzmer, J. Molecular Architecture and Function of Polymeric Oriented Systems: Models for the Study of Organization, Surface Recognition, and Dynamics of Biomembranes. *Angew. Chem., Int. Ed. Engl.* **1988**, *27*, 113–158.
2. Kuna, J. J.; Voïtchovsky, K.; Singh, C.; Jiang, H.; Mwenifumbo, S.; Ghorai, P. K.; Stevens, M. M.; Glotzer, S. C.; Stellacci, F. The Effect of Nanometer-Scale Structure on Interfacial Energy. *Nat. Mater.* **2009**, *8*, 837–842.
3. Pasquato, L.; Rancan, F.; Scrimin, P.; Mancin, F.; Frigeri, C. N-Methylimidazole-Functionalized Gold Nanoparticles as

Catalysts of the Cleavage of a Carboxylic Acid Ester. *Chem. Commun.* **2000**, 2253–2254.

4. Manea, F.; Bodar Houillon, F.; Pasquato, L.; Scrimin, P. Nanozymes: Gold-Nanoparticles-Based Transphosphorylation Catalysts. *Angew. Chem., Int. Ed.* **2004**, *43*, 6165–6169.
5. Pengo, P.; Polizzi, S.; Pasquato, L.; Scrimin, P. Carboxylate-Imidazole Cooperativity in Dipeptide-Functionalized Gold Nanoparticles with Esterase-like Activity. *J. Am. Chem. Soc.* **2005**, *127*, 1616–1617.
6. Pengo, P.; Baltzer, L.; Pasquato, L.; Scrimin, P. Substrate Modulation of the Activity of an Artificial Nanoesterase Made of Peptide-Functionalized Gold Nanoparticles. *Angew. Chem., Int. Ed.* **2007**, *46*, 400–404.
7. Zaupa, G.; Mora, C.; Bonomi, R.; Prins, L. J.; Scrimin, P. Catalytic Self-Assembled Monolayers on Au Nanoparticles: The Source of Catalysis of a Transphosphorilation Reaction. *Chem.—Eur. J.* **2011**, *17*, 4879–4889.
8. Bonomi, R.; Selvestrel, F.; Lombardo, V.; Sissi, C.; Polizzi, S.; Mancin, F.; Tonellato, U.; Scrimin, P. Phosphate Diester and DNA Hydrolysis by a Multivalent, Nanoparticle-Based Catalyst. *J. Am. Chem. Soc.* **2008**, *130*, 15744–15745.
9. Belser, T.; Jacobsen, E. N. Cooperative Catalysis in the Hydrolytic Kinetic Resolution of Epoxides by Chiral [(salen)Co(III)] Complexes Immobilized on Gold Colloids. *Adv. Synth. Catal.* **2008**, *350*, 967–971.
10. Fantuzzi, G.; Pengo, P.; Gomilla, R.; Ballester, P.; Hunter, C. A.; Pasquato, L.; Scrimin, P. Multivalent Recognition of Bis- and Tris-Zn-Porphyrins by N-Methylimidazole Functionalized Gold Nanoparticles. *Chem. Commun.* **2003**, 1004–1005.
11. Bowman, M.-C.; Ballard, T. E.; Ackerson, C. J.; Feldheim, D. L.; Margolis, D. M.; Melander, C. Inhibition of HIV Fusion with Multivalent Gold Nanoparticles. *J. Am. Chem. Soc.* **2008**, *130*, 6896–6897.
12. Verma, A.; Uzun, O.; Hu, Y.; Hu, Y.; Han, H.-S.; Watson, N.; Chen, S.; Irvine, D. J.; Stellacci, F. Surface-Structure-Regulated Cell-Membrane Penetration by Monolayer-Protected Nanoparticles. *Nat. Mater.* **2008**, *7*, 588–595.
13. De Vries, G. A.; Brunnbauer, M.; Hu, Y.; Jackson, A. M.; Long, B.; Neltner, B. T.; Uzun, O.; Wunsh, B. H.; Stellacci, F. Divalent Metal Nanoparticles. *Science* **2007**, *315*, 358–361.
14. Perepichka, D. F.; Rosei, F. Metal Nanoparticles: from “Artificial Atoms” to “Artificial Molecules”. *Angew. Chem., Int. Ed.* **2007**, *46*, 6006–6008.
15. Hermans, T. M.; Broeren, M. A. C.; Gomopoulos, N.; van der Schoot, P.; van Genderen, M. H. P.; Sommerdijk, N. A. J. M.; Fytas, G.; Meijer, E. W. Self-Assembly of Soft Nanoparticles with Tunable Patchiness. *Nat. Nanotechnol.* **2009**, *4*, 721–726.
16. Akcora, P.; Liu, H.; Kumar, S. K.; Moll, J.; Li, Y.; Benicewicz, B. C.; Schadler, L. S.; Acehan, D.; Panagiotopoulos, A. Z.; Pryamitsyn; *et al.* Anisotropic Self-Assembly of Spherical Polymer-Grafted Nanoparticles. *Nat. Mater.* **2009**, *8*, 354–359.
17. Ruzicka, B.; Zaccarelli, E.; Zulian, L.; Angelini, R.; Sztucki, M.; Moussaïd, A.; Narayanan, T.; Sciortino, F. Observation of Empty Liquids and Equilibrium Gels in a Colloidal Clay. *Nat. Mater.* **2011**, *10*, 56–60.
18. Mager, M. D.; LaPointe, V.; Stevens, M, M. Exploring and Exploiting Chemistry at the Cell Surface. *Nat. Chem.* **2011**, *3*, 582–589.
19. Daniel, M.-C.; Astruc, D. Gold Nanoparticles: Assembly, Supramolecular Chemistry, Quantum-Size-Related Properties, and Applications toward Biology, Catalysis, and Nanotechnology. *Chem. Rev.* **2004**, *104*, 293–346.
20. Gentilini, C.; Pasquato, L. Morphology of Mixed-Monolayers Protecting Metal Nanoparticles. *J. Mater. Chem.* **2010**, *20*, 1403–1412.
21. Jackson, A. M.; Myerson, J. W.; Stellacci, F. Spontaneous Assembly of Subnanometre-Ordered Domains in the Ligand Shell of Monolayer-Protected Nanoparticles. *Nat. Mater.* **2004**, *3*, 330–336.
22. Jadzinsky, P. D.; Calero, G.; Ackerson, C. J.; Bushnell, D. A.; Kornberg, R. D. Structure of a Thiol Monolayer-Protected Gold Nanoparticle at 1.1 Å Resolution. *Science* **2007**, *318*, 430–433.
23. Lucarini, M.; Pasquato, L. ESR Spectroscopy as a Tool to Investigate the Properties of Self-Assembled Monolayers Protecting Gold Nanoparticles. *Nanoscale* **2010**, *2*, 668–676.
24. Lucarini, M.; Franchi, P.; Pedulli, G. F.; Pengo, P.; Scrimin, P.; Pasquato, L. EPR Study of Dialkyl Nitroxides as Probes to Investigate the Exchange of Solutes between the Ligand Shell of Monolayers of Protected Gold Nanoparticles and Aqueous Solutions. *J. Am. Chem. Soc.* **2004**, *126*, 9326–9329.
25. Lucarini, M.; Franchi, P.; Pedulli, G. F.; Gentilini, C.; Polizzi, S.; Pengo, P.; Scrimin, P.; Pasquato, L. Effect of Core Size on the Partition of Organic Solutes in the Monolayer of Water-Soluble Nanoparticles: An ESR Investigation. *J. Am. Chem. Soc.* **2005**, *127*, 16384–16385.
26. Gentilini, C.; Evangelista, F.; Rudolf, P.; Franchi, P.; Lucarini, M.; Pasquato, L. Water-Soluble Gold Nanoparticles Protected by Fluorinated Amphiphilic Thiolates. *J. Am. Chem. Soc.* **2008**, *130*, 15678–15682.
27. Pradhan, S.; Brown, L. E.; Konopelski, J. P.; Chen, S. Janus Nanoparticles: Reaction Dynamics and NOESY Characterization. *J. Nanopart. Res.* **2009**, *11*, 1895–1903.
28. Guarino, G.; Rastrelli, F.; Scrimin, P.; Mancin, F. Lanthanide-Based NMR: A Tool to Investigate Component Distribution in Mixed-Monolayer-Protected Nanoparticles. *J. Am. Chem. Soc.* **2012**, *134*, 7200–7203.
29. Duchesne, L.; Wells, G.; Fernig, D. G.; Harris, S. A.; Levy, R. Supramolecular Domains in Mixed Peptide Self-Assembled Monolayers on Gold Nanoparticles. *ChemBioChem* **2008**, *9*, 2127–2134.
30. Bonomi, R.; Cazzolaro, A.; Prins, L. J. Assessment of the Morphology of Mixed SAMs on Au Nanoparticles Using a Fluorescent Probe. *Chem. Commun.* **2011**, *47*, 445–447.
31. For silver NPs: Stewart, A.; Zheng, S.; McCourt, M. R.; Bell, S. E. J. Controlling Assembly of Mixed Thiol Monolayers on Silver Nanoparticles to Tune Their Surface Properties. *ACS Nano* **2012**, *6*, 3718–3726.
32. Sing, C.; Ghorai, P. K.; Horsch, M. A.; Jackson, A. M.; Larson, R. G.; Stellacci, F.; Glotzer, S. C. Entropy-Mediated Patterning of Surfactant-Coated Nanoparticles and Surfaces. *Phys. Rev. Lett.* **2007**, *99*, 226106.
33. Ghorai, P. K.; Glotzer, S. C. Atomistic Simulation Study of Striped Phase Separation in Mixed-Ligand Self-Assembled Monolayer Coated Nanoparticles. *J. Phys. Chem. C* **2010**, *114*, 19182–19187.
34. Mukerjee, P.; Yang, A. Y. S. Nonideality of Mixing of Micelles of Fluorocarbon and Hydrocarbon Surfactants and Evidence of Partial Miscibility from Differential Conductance Data. *J. Phys. Chem.* **1976**, *80*, 1388–1390.
35. Kunitake, T.; Tawaki, S.; Nakashima, N. Excimer Formation and Phase Separation of Hydrocarbon and Fluorocarbon Bilayer Membranes. *Bull. Chem. Soc. Jpn.* **1983**, *56*, 3235–3242.
36. Elbert, R.; Folda, T.; Ringsdorf, H. Saturated and Polymerizable Amphiphiles with Fluorocarbon Chains. Investigation in Monolayers and Liposomes. *J. Am. Chem. Soc.* **1984**, *106*, 7687–7692.
37. Riess, J. C. Florous Micro- and Nanophases with a Biomedical Perspective. *Tetrahedron* **2002**, *58*, 4113–4131, and references therein.
38. See also for example: Yoder, N. C.; Kalsani, V.; Schuy, S.; Vogel, R.; Janshoff, A.; Kumar, K. Nanoscale Patterning in Mixed Fluorocarbon-Hydrocarbon Phospholipid Bilayers. *J. Am. Chem. Soc.* **2007**, *129*, 9037–9043, and references therein.
39. Takiue, T.; Vollhardt, D. Miscibility of Alkanol and Fluoroalkanol in Langmuir Film at the Air/Water Interface. *Colloids Surf., A* **2002**, *198–200*, 797–804.
40. Zhu, B.-Y.; Zhang, P.; Wang, R.-X.; Liu, Z.-F.; Lai, L.-H. Phase Separation and Crystallization in Mixed Monolayers of FC and HC Surfactants. *Colloids Surf., A* **1999**, *157*, 63–71.
41. Bilgiçer, B.; Kumar, K. *De Novo* Design of Defined Helical Bundles in Membranes Environments. *Proc. Natl. Acad. Sci. U. S. A.* **2004**, *101*, 15324–15329.
42. Li, Z.; Kesselman, E.; Talmon, Y.; Hillmyer, M. A.; Lodge, T. P. Multicompartment Micelles from ABC Miktoarm Stars in Water. *Science* **2004**, *306*, 98–101.

43. Singh, C.; Jackson, A. M.; Stellacci, F.; Glotzer, S. C. Exploiting Substrate Stress to Modify Nanoscale SAM Patterns. *J. Am. Chem. Soc.* **2009**, *131*, 16377–16379.
44. Gentilini, C.; Franchi, P.; Mileo, E.; Polizzi, S.; Lucarini, M.; Pasquato, L. Formation of Patches on 3D SAMs Driven by Thiols with Immiscible Chains Observed by ESR Spectroscopy. *Angew. Chem., Int. Ed.* **2009**, *48*, 3060–3064.
45. Pengo, P.; Polizzi, S.; Battagliarin, M.; Pasquato, L.; Scrimin, P. Synthesis, Characterization and Properties of Water-Soluble Gold Nanoparticles with Tunable Core Size. *J. Mater. Chem.* **2003**, *13*, 2471–2478.
46. Uzun, O.; Hu, Y.; Verma, A.; Chen, S.; Centrone, A.; Stellacci, F. Water-Soluble Amphiphilic Gold Nanoparticles with Structured Ligand Shells. *Chem. Commun.* **2008**, 196–198.
47. Carney, R. P.; DeVries, G. A.; Dubois, C.; Kim, H.; Kim, J. Y.; Singh, C.; Ghorai, P. K.; Tracy, J. B.; Stiles, R. L.; Murray, R. W.; *et al.* Size Limitations for the Formation of Ordered Striped Nanoparticles. *J. Am. Chem. Soc.* **2008**, *130*, 798–799.
48. For NPs **8**, the measure of ΔG is compatible with both nanoparticles having a large number of patches formed by a small number of molecules or nanoparticles having small number of patches with a large number of molecules. In the latter case, however, two or more radicals should be located in the same patches when $\chi = 0.95$. This is clearly not possible because the ESR spectrum does not show any evidence of electron exchange between two or more radicals.
49. The linearity of eq 1, relating the two quantities ΔG and X_H, has been checked by simulating the low-field lines of the ESR spectrum of **3** at different X_H values and by plotting the field separation ΔG extracted from these spectra *vs* X_H. As expected, a good linear relationship was observed (see Figures S7 and S8 in the Supporting Information).
50. Mezzina, E.; Cruciani, F.; Pedulli, G. F.; Lucarini, M. Nitroxide Radicals as Probes for Exploring the Binding Properties of the Curcubit[7]uril Host. *Chem.—Eur. J.* **2007**, *13*, 7223–7233.
51. Centrone, A.; Penzo, E.; Sharma, M.; Myerson, J. W.; Jackson, A. M.; Marzari, N.; Stellacci, F. The Role of Nanosctructure in the Wetting Behavior of Mixed-Monolayer-Protected Metal Nanoparticles. *Proc. Natl. Acad. Sci. U. S. A.* **2008**, *105*, 9886–9891.
52. By considering the uncertainties in the measure of both ΔG and in K_{mix} the errors associated with the measure of K_H and K_F are larger when χ is equal to 0.80 and 0.95.